

# Bipolar Organic Cathodes for Stable and Sustainable Na-Ion and Rechargeable Al Batteries

Eric Youngsam Kim,<sup>[a]</sup> Kaitlyn Vi-khanh Ta,<sup>[a]</sup> Fu Chen,<sup>[b]</sup> Zhenzhen Yang,<sup>[c]</sup> Yun Yu,<sup>[a, d]</sup> and Chao Luo<sup>\*[a, d, e]</sup>

Bipolar organic materials have emerged as promising cathode materials for rechargeable batteries because of their high voltage and high capacity. However, they suffer from poor cyclic stability and slow reaction kinetics. In this work, we designed and synthesized two bipolar organic cathode materials, containing carbonyl (n-type) and amine (p-type) functional groups, as well as extended conjugation structures, for Na-ion batteries (NIBs) and rechargeable aluminum batteries (RABs). As universal electrode materials, bipolar organic materials exhibited exceptional electrochemical performance in terms of high capacity, high voltage, long cycle life, and fast rate capability. The extended conjugation structures in backbones of the

bipolar organic materials facilitate the  $\pi-\pi$  stacking with graphene, playing a critical role in the high performance. Furthermore, the formation of a stable and robust NaF-rich cathode electrolyte interphase was shown to stabilize the bipolar organic cathode in NIBs. Electrochemical kinetic measurements reveal that both functional groups undergo reversible redox reactions. Specifically, the electron transfer rate constant of the p-type amine group is one order of magnitude higher than that of the n-type carbonyl group. These results highlight the efficacy of developing bipolar organic materials for achieving high-performance organic cathode in NIBs and RABs.

## Introduction

To achieve carbon neutrality and energy sustainability, there will be a significant reduction in the use of fossil fuels, accompanied with an increasing reliance on renewable energies and electrochemical energy storage systems.<sup>[1,2]</sup> To date, lithium-ion batteries (LIBs) are dominant energy storage devices for portable electronics, electric transportation, and grid-scale energy storage. However, state-of-the-art LIBs cannot satisfy the requirements for net-zero carbon emissions due to high cost and low abundance of transition metals (Ni and Co), as well as the limited capacity of the cathodes.<sup>[3-6]</sup> Consequently, the design of advanced cathode materials based on affordable, abundant, and high-capacity resources for battery systems beyond LIBs is paramount to address these challenges. Among emerging rechargeable battery systems, Na-ion batteries (NIBs)

and rechargeable Al batteries (RABs) stand out because of low cost and high abundance of sodium and aluminum resources, as well as high capacity of carbon and Na/Al metal anodes. However, due to the larger ion size and complicated intercalation chemistries, inorganic cathode materials do not extend their high performance from LIBs to NIBs and RABs. The electrochemical performance of NIBs and RABs still cannot compete with LIBs. To enhance the performance and realize practical applications, developing advanced cathode materials for NIBs and RABs is critical.<sup>[7-9]</sup>

As universal electrode materials, organic compounds have demonstrated promising performances as cathode materials in NIBs and RABs. Further development and application of organic electrode materials (OEMs) are impeded by their low electronic conductivity and high solubility in the electrolyte, which result in slow reaction kinetics and fast capacity loss upon cycling.<sup>[10,11]</sup> To address these challenges, a variety of methods such as salinization, polymerization, electrolyte design, surface coating, etc. have been leveraged.<sup>[12]</sup> Significant progress and structure design rationale were achieved to obtain high-performance organic electrodes for NIBs and RABs in the last decade. So far, OEMs are classified into three categories, depending on redox reaction mechanisms and functional groups: negative (n)-type, positive (p)-type, and bipolar materials.<sup>[13,14]</sup> The n-type OEMs such as carbonyl-, azo-, or imine-based organic molecules/polymers can be reduced to create negative charged states by accepting electrons/cations. The p-type OEMs such as thioether-, nitroxyl radical-, or tertiary amines-based organic molecules/polymers undergo oxidation reactions to generate positive charged states by losing electrons while gaining anions from the electrolyte.<sup>[15,16]</sup> The p-type organic electrodes exhibit high redox voltage but suffer from low specific capacity.<sup>[17]</sup> The n-type organic electrodes exhibit low redox voltage but deliver

[a] E. Youngsam Kim, K. Vi-khanh Ta, Prof. Y. Yu, Prof. C. Luo  
Department of Chemistry and Biochemistry, George Mason University, Fairfax, VA 22030, USA

[b] Dr. F. Chen  
Department of Chemistry and Biochemistry, University of Maryland, College Park, MD, 20742, USA

[c] Dr. Z. Yang  
Chemical Sciences and Engineering Division, Argonne National Laboratory, Lemont, IL, 60439, USA

[d] Prof. Y. Yu, Prof. C. Luo  
Quantum Science & Engineering Center, George Mason University, Fairfax, VA, 22030, USA

[e] Prof. C. Luo  
Department of Chemical, Environmental, and Materials Engineering, University of Miami, Coral Gables, FL, 33146, USA  
E-mail: cxl1763@miami.edu

 Supporting information for this article is available on the WWW under <https://doi.org/10.1002/batt.202400325>

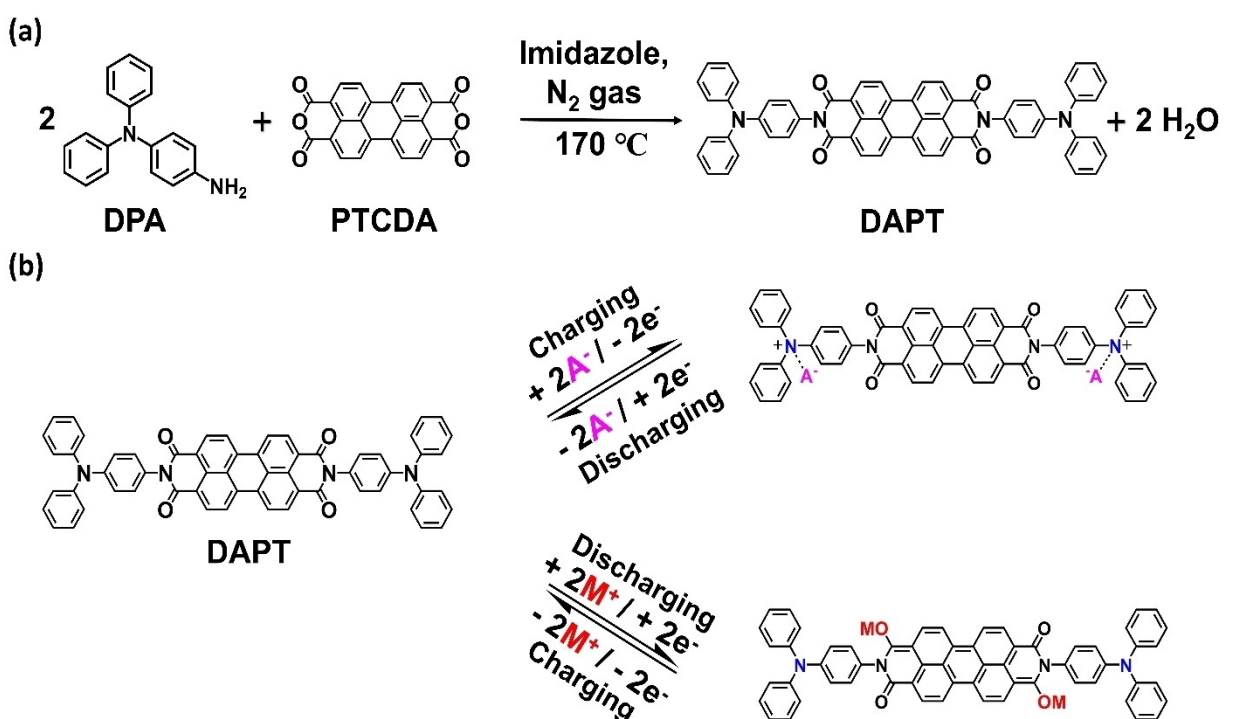
high specific capacity. To develop high-voltage and high-capacity cathode materials for NIBs and RABs, bipolar OEMs with multiple n-type and p-type functional groups offer opportunities.<sup>[18,19]</sup> An in-depth understanding and rational design of bipolar OEMs are vital for achieving high-performance organic NIBs and RABs.

Herein, we designed two bipolar OEMs as cathode materials in NIBs and RABs, which contain carbonyl and tertiary amine functional groups. The bipolar OEMs named as DAPT and NTDA were synthesized by a one-pot condensation reaction between pernylenetetracarboxylic dianhydride (PTCDA)/ naphthalenetracarboxylic dianhydride (NTCDA) and N1, N1-diphenylbenzene-1,4-diamine (DPA) as shown in Scheme 1a and S1a. Their reaction mechanisms in NIBs and RABs are shown in Scheme 1b and S1b. In DAPT and NTDA, n-type carbonyl groups reversibly react with metal ions/complex ( $\text{Na}^+$ , or  $\text{AlCl}_2^+$ ), while p-type amine group reversibly react with anions such as  $\text{PF}_6^-$ , or  $\text{AlCl}_4^-$ .<sup>[20,21]</sup> The extended conjugation structures in DAPT and NTDA not only reduce the solubility but also form  $\pi$ - $\pi$  stacking with single-layer graphene in the cathodes, enhancing the conductivity and cyclic stability of cathodes. Therefore, the bipolar OEM, DAPT, exhibited high specific capacity, long cycle life, and fast rate capability, representing promising cathode materials in rechargeable batteries beyond LIBs.

## Results and Discussion

The bipolar OEMs, DAPT and NTDA, were synthesized through a one-pot condensation method. To verify their structures, Four-

ier-transform infrared (FTIR) spectroscopy, Raman spectroscopy, scanning electron microscopy (SEM), solid-state nuclear magnetic resonance (NMR), and X-ray photoelectron microscopy (XPS) were utilized. In FTIR spectra, the N–H peaks are detected at  $3400\text{ cm}^{-1}$  and  $3300\text{ cm}^{-1}$  from the amino group in DPA. These peaks disappear in DAPT and NTDA (Figure 1a and S1a), indicating the success of the condensation reaction. In the Raman spectra (Figure 1b), DAPT and NTDA each displayed a distinct peak at  $1710\text{ cm}^{-1}$ , corresponding to the C=O vibrational mode. Single medium-intensity peak at  $1578\text{ cm}^{-1}$  was observed, indicating vibrations of C–C and C=C bonds. Furthermore, two high-intensity peaks at  $1294\text{ cm}^{-1}$  and  $1377\text{ cm}^{-1}$  were induced through  $\text{C}_{\text{ar}}-\text{H}$  vibration. Additionally, the single small peak at  $1053\text{ cm}^{-1}$  indicated the C–N bond vibration.<sup>[22–24]</sup> SEM images of DPPT and DPNT (Figure 1c and S1b) showed rod-shaped and irregular-shaped microparticles, respectively. To further confirm the chemical structure, solid state NMR was used. In the  $^{13}\text{C}$  solid-state NMR spectrum (Figure 1d), carbonyl carbon is detected at  $\sim 160\text{ ppm}$ . The aromatic carbons bonded with N are represented at  $\sim 145\text{ ppm}$ , while other aromatic carbons are exhibited in the wide range from  $115$  to  $130\text{ ppm}$ . In the  $^{15}\text{N}$  solid-state NMR spectrum (Figure 1e), two peaks at  $169$  and  $167\text{ ppm}$  are from nitrogen bonded with carbonyl carbon in the imide moieties, and another peak at  $85\text{ ppm}$  indicates the nitrogen in the amine moieties. The  $^{17}\text{O}$  solid-state NMR spectrum (Figure 1f) showed a single peak at  $378.9\text{ ppm}$ , corresponding to carbonyl oxygen.<sup>[25–27]</sup> Additionally, the XPS results (Figure 1g–i) further confirm the chemical structure of DAPT. In the C 1s spectrum, the highest peak at  $284.7\text{ eV}$  is attributed to C–C/C=C bonds,



**Scheme 1.** (a) Synthetic procedure of DAPT; (b) the proposed reaction mechanism of DAPT, where M represents Na ions/Al complex, and A represents anion such as  $\text{PF}_6^-/\text{AlCl}_4^-$ .

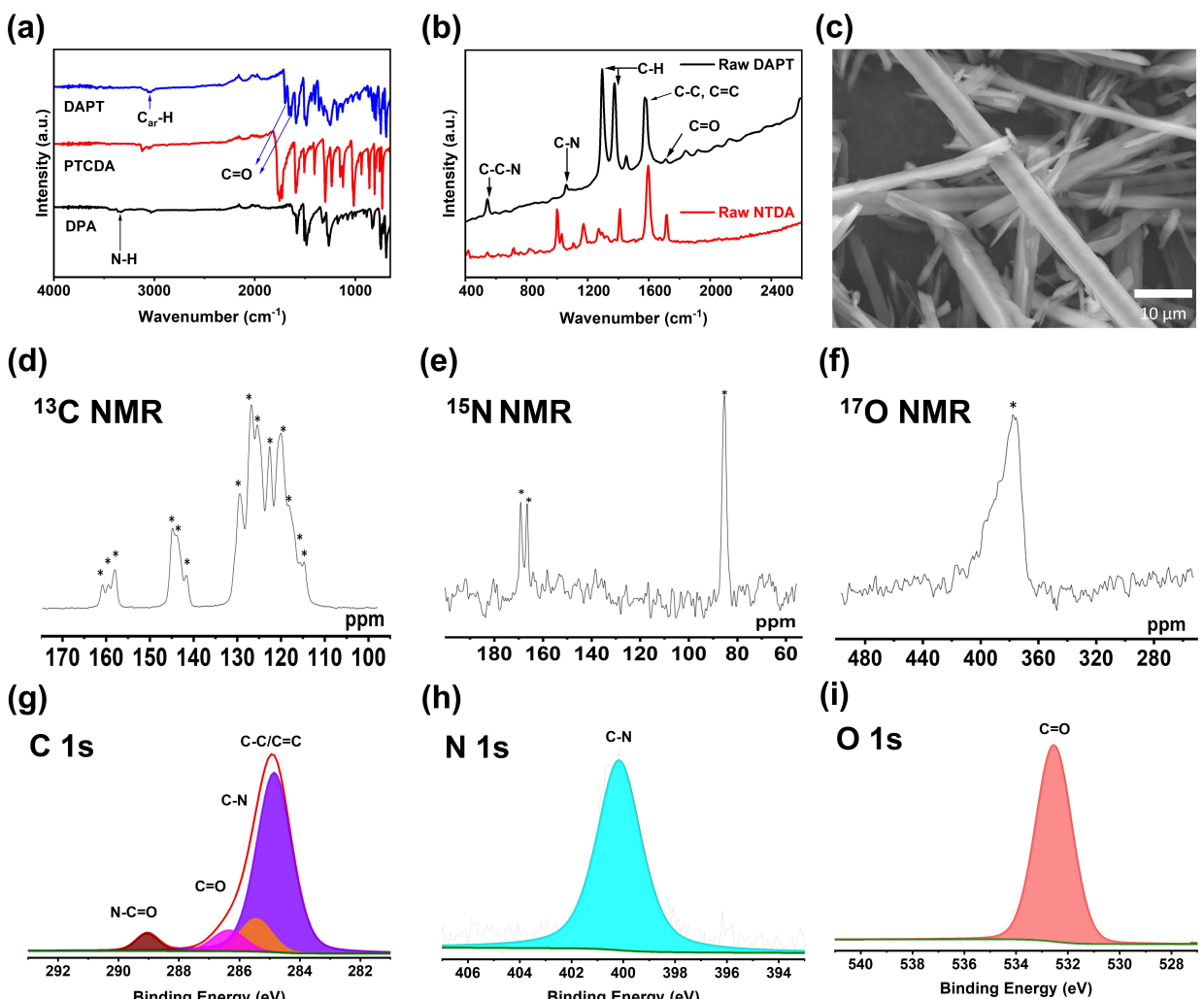


**Figure 1.** Material characterizations for raw-DAPT: (a) FT-IR spectra, (b) Raman spectra of raw-DAPT powder and raw NTDA, (c) SEM image for raw-DAPT powder, (d)  $^{13}\text{C}$ , (e)  $^{15}\text{N}$ , (f)  $^{17}\text{O}$  solid-state NMR, (g) C 1s, (h) N 1s, (i) O 1s XPS spectra for raw-DAPT.

while three smaller peaks at 285.6, 286.5, and 289.1 eV indicate the C–N, C=O, and N–C=O bonds, respectively. Similarly, the N 1s and O 1s spectra each display a single peak at 399.6 and 532.4 eV, representing C–N and C=O bonds, respectively.<sup>[28–30]</sup> These XPS results collectively validate the structural composition of DAPT.

To evaluate the electrochemical performances of DAPT and NTDA in NIBs, 1.0 M NaPF<sub>6</sub> in ethylene carbonate (EC): diethylene carbonate (DEC) (1:1/V) electrolyte was utilized. Before the electrochemical measurements, we assessed the solubility of the electrodes in the electrolyte. DAPT and NTDA electrodes were immersed in the electrolyte solution and organic solvents (EC: DEC, 1:1/V) for 24 hours. Subsequently, the liquid solutions were sealed in the glovebox to prevent air contact, and then UV-vis spectroscopy was conducted. In the UV-vis spectra (Figure S2), all spectra show minimal absorption close to 0 in the range of 380–1300 nm, indicating that DAPT and NTDA are insoluble in the electrolyte.

Electrochemical performances of DAPT and NTDA cathodes with graphene in NIBs were investigated by galvanostatic charge-discharge tests. The cutoff window for both electrodes

are 1.0–3.9 V. The galvanostatic charge-discharge curves of DAPT exhibit reversible redox plateaus centered at 2.2 V and 3.6 V (Figure 2a). The redox processes associated with the two plateaus are attributed to reactions of carbonyl groups and amine groups, respectively, which is verified in the undermentioned discussions. The first discharge curve was shorter than subsequent discharge curves because the open-circuit potential of NIB was around 2.1 V. Consequently, only carbonyl functional group underwent redox reaction during the first discharge (2.1 V–1 V). In the cyclic performance at 50 mAh g<sup>-1</sup>, the initial reversible capacity of the DAPT cathode was 169.3 mAh g<sup>-1</sup>. After 500 cycles, the specific capacity was retained at 143.9 mAh g<sup>-1</sup> (Figure 2b), representing a slow capacity decay rate of 0.03% per cycle. To further study kinetics, a high-current-density galvanostatic charge-discharge and long-cycling performances at 500 mAh g<sup>-1</sup> were performed (Figure 2c). The CV peaks in Figure 2e are well corresponded with the redox plateaus in Figure 2a and 2c, showing the carbonyl reaction with Na<sup>+</sup> and amine reaction with anions. The initial capacity at 500 mAh g<sup>-1</sup> was 160 mAh g<sup>-1</sup>. After 1000 cycles, the specific

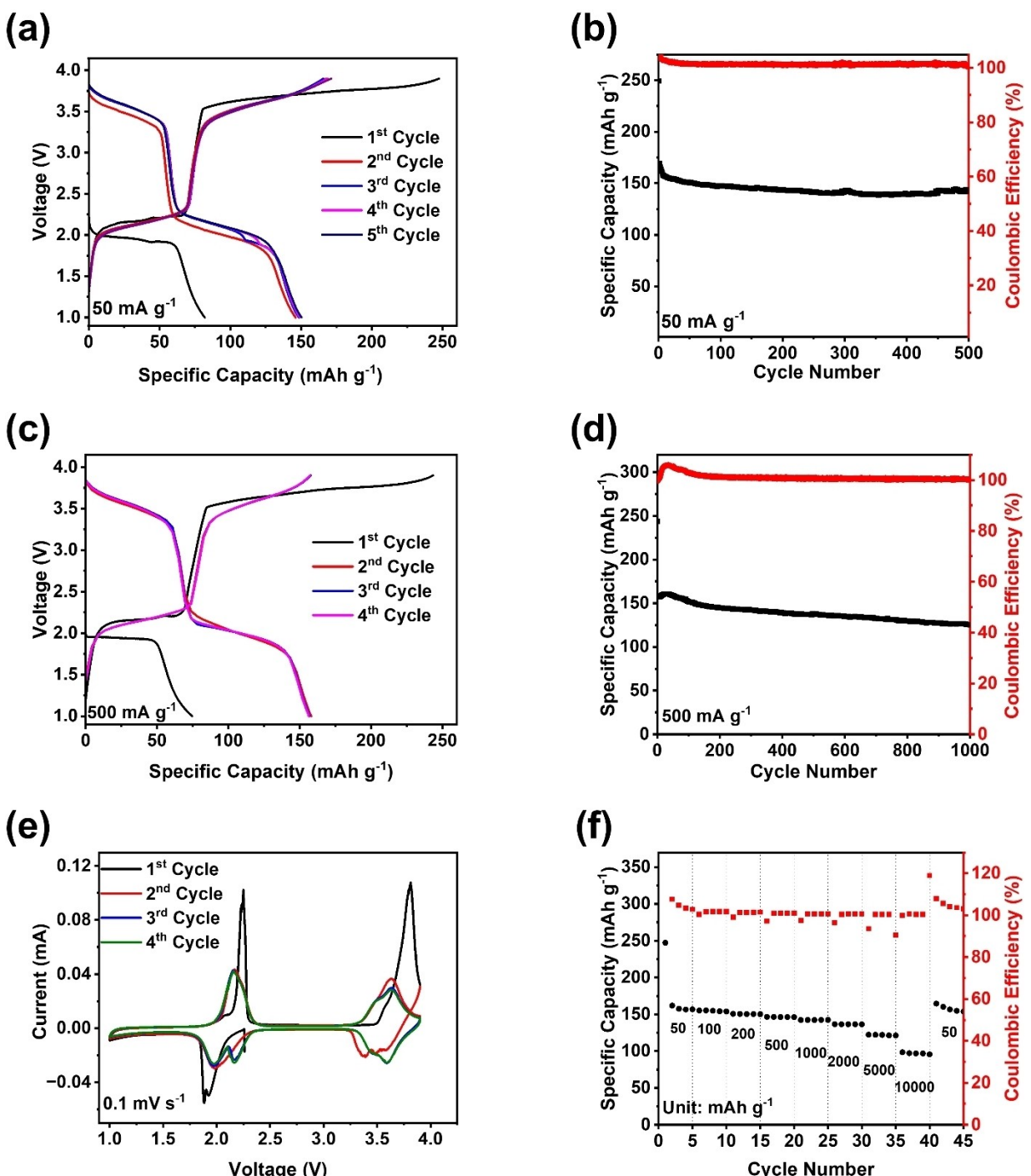


**Figure 2.** Electrochemical performances of the DAPT cathode with graphene in NIBs. (a) Galvanostatic charge-discharge curves at  $50 \text{ mA g}^{-1}$ ; (b) cycling performances at  $50 \text{ mA g}^{-1}$ ; (c) galvanostatic charge-discharge curves at  $500 \text{ mA g}^{-1}$ ; (d) cycling performances at  $500 \text{ mA g}^{-1}$ ; (e) cyclic voltammograms at  $0.1 \text{ mV s}^{-1}$ ; (f) rate capability at various current densities.

capacity reduced to  $118.8 \text{ mAh g}^{-1}$  with a slow capacity decay rate of  $0.0258\%$  per cycle (Figure 2d). The galvanostatic charge-discharge curves for DAPT without graphene showed two pairs of redox plateaus at similar potentials,  $3.6 \text{ V}$  and  $2.2 \text{ V}$  (Figure S3a). However, it delivered lower electrochemical performance than that of the DAPT cathode with graphene. The DAPT cathode without graphene delivered an initial capacity of  $110.1 \text{ mAh g}^{-1}$ , and it decreased to  $79.1 \text{ mAh g}^{-1}$  after 100 cycles

(Figure S3b), representing a capacity decay rate of  $0.282\%$  per cycle. The higher stability of the DAPT cathode with graphene is attributed to the  $\pi-\pi$  stacking between the conjugation structures in DAPT and graphene, which not only enhances the specific capacity but also improves the stability of the electrode.<sup>[31]</sup> Meanwhile, NTDA exhibited different electrochemical behaviors from DAPT as shown in Figure S4a. One pair of redox plateaus at  $2.1 \text{ V}$  and  $2.5 \text{ V}$  can be observed for the NTDA

electrode with graphene, corresponding to two pairs of redox peaks at 1.6/2.2 V and 1.8/2.6 V in the cyclic voltammogram (Figure S4b). The redox peaks are close to each other and merged into one pair of charge/discharge plateaus in Figure S4a. The initial capacity of NTDA was  $143.1 \text{ mAh g}^{-1}$ , and it was gradually reduced to  $71.6 \text{ mAh g}^{-1}$  after 500 cycles (Figure S4c), representing a capacity decay rate of 0.1% per cycle. The primary cause of the inferior electrochemical performances compared to DAPT is the difference in the structure of conjugation systems. DAPT possesses larger extended conjugated structures than NTDA, leading to lower solubility and higher stability. These results emphasize the critical role of the conjugation structure in the electrochemical performance.<sup>[32]</sup> Given DAPT's excellent electrochemical performance, further investigations were conducted using rate capability tests. The rate capability of DAPT was evaluated at incremental current densities from  $50 \text{ mA g}^{-1}$  to  $10 \text{ A g}^{-1}$  (Figure 2f). The initial specific capacity at  $50 \text{ mA g}^{-1}$  was  $157.6 \text{ mAh g}^{-1}$ . After recovering from the highest current density (36–40 cycles) to initial current density (41–45 cycles), the specific capacity is retained at  $156.7 \text{ mAh g}^{-1}$  with 99.4% capacity retention, demonstrating fast and robust kinetics. Hence, these results prove that DAPT represents a high-performance cathode in terms of high capacity, long cycle life, and fast-charging capability.

To further investigate reaction kinetics of the DAPT cathode, we employed galvanostatic intermittent titration technique (GITT), electrochemical impedance spectroscopy (EIS), and cyclic voltammetry (CV) at various scan rates, along with analyzing peak separation from CV data. GITT involved alternating cycles of charging and discharging at  $50 \text{ mA g}^{-1}$  for 30 minutes, with intervals of 3 hours of rest. As shown in Figure 3a, small overpotentials are observed for carbonyl reaction with  $\text{Na}^+$  centered around 2 V, while the overpotentials for the amine reaction with anions are larger. Through the analysis of the electrode potential measured during the current pulse (Table S1), the diffusion coefficient of  $\text{Na}^+$  and  $\text{PF}_6^-$  were determined to be  $1.73 \times 10^{-9} \text{ cm}^2 \text{s}^{-1}$  and  $1.06 \times 10^{-9} \text{ cm}^2 \text{s}^{-1}$ , respectively. The diffusivity of  $\text{Na}^+$  ions is 65% greater than that of  $\text{PF}_6^-$ , indicating that the material exhibits higher cationic conductivity compared to the counter anion. In the EIS spectra, the depressed semi-circle of the pristine DAPT cathode for the interphase resistance is  $1810 \Omega$  (Figure 3b). After the first cycle, it was dramatically reduced to  $116.8 \Omega$  and retained at  $94.6 \Omega$  and  $68.53 \Omega$  after 5 cycles and 10 cycles (Figure S5). The small and stable interfacial resistance suggests high stability of the interphase between the DAPT cathode and the electrolyte, which is critical for the cycle life of the DAPT cathode.<sup>[33,34]</sup>

To evaluate the polarization of DAPT, CV at various rates from  $1.0 \text{ mVs}^{-1}$  to  $5.0 \text{ mVs}^{-1}$  was performed. As shown in Figure 3c, the cathodic and anodic curves exhibited slight shifts as scan rates were increased from 1.0 to  $5.0 \text{ mVs}^{-1}$ . This result demonstrated that DAPT does not perform significant polarization with elevated scan rates. Two pairs of cathodic and anodic peaks centered at 2.1 V (vs  $\text{Na}/\text{Na}^+$ ) and 3.6 V (vs  $\text{Na}/\text{Na}^+$ ) are attributed to the reduction and oxidation of carbonyl groups and the amine groups, respectively. The natural logarithms of these peak current values were plotted against

the natural logarithms of scan rates (Figure 3d). The slopes of the anodic and cathodic dependance for the carbonyl reaction were determined to be 0.8641 and 0.8100, respectively. For the amine reaction, the slope values were 0.9049 and 0.9039, respectively. The slope values close to 1 suggested that reaction kinetics is dominated by surface reaction and exhibits a pseudocapacitive behavior.<sup>[35,36]</sup>

To further analyze reaction kinetics for each functional group, the difference between the cathodic peak potential and the anodic peak potential ( $\Delta E_p$ ) was examined (Figure 3e). Smaller peak separations at a given scan rate indicate faster electron transfer kinetics. Herein, the Butler–Volmer electron transfer formalism for surface-confined electrode reactions is used to quantify the intrinsic reactivity of both functional groups.<sup>[37,38]</sup> Transfer coefficient ( $\alpha$ ) and number of electrons transfer ( $n$ ) involved in the electrode reaction for carbonyl and amine groups were calculated using peak potential versus log scan rate (Figure S6). Based on the extracted parameters and the  $\Delta E_p$  values in the Figure 3e, the standard reaction constants ( $k^o$ ) for the carbonyl and amine groups were deciphered using the analytical equation introduced by Lavorin.<sup>[39]</sup> In the Figure 3f, we plotted the calculated  $k^o$  as a function of the scan rate. Almost constant  $k^o$  values were obtained at various scan rates, justifying our assumption that the redox processes are surface-confined. The  $k^o$  values for the carbonyl reaction was determined to be  $(7.0 \pm 0.1) \times 10^{-4} \text{ s}^{-1}$ , while the  $k^o$  for amine reaction is  $(6.1 \pm 0.1) \times 10^{-3} \text{ s}^{-1}$ . The intrinsic electron transfer rate of the amine group is almost an order of magnitude higher than that of the carbonyl group, as indicated by their  $k^o$  values. Additionally, EIS was conducted following partial discharging to 2.0 V (carbonyl reaction) and charging to 3.6 V (amine reaction) (Figure S6c and S6d). The Nyquist plots indicate that the charge transfer resistance of the amine reaction is 9.4 times lower than that of the carbonyl reaction, in consistency with the  $k^o$  values determined in Figure 3f. We attribute the discrepancy in reactivity to the ion solvation effects within the electrolyte.<sup>[40]</sup> Each dissolved salt-ion forms distinct interactions with electrolyte solvents, including coordinate bonds, hydrogen bonds, and Van der Waals forces. Specifically,  $\text{Na}^+$  ions interact with organic solvents by forming coordinate bonds through the donation of lone electron pairs, typically from oxygen in EC and DEC. In contrast,  $\text{PF}_6^-$  ions establish interactions with organic solvents through hydrogen bonds (F–H) and Van der Waals forces.<sup>[41,42]</sup> Among these interactions, coordinate bonds exhibit greater strength compared to other types. These robust interactions impede desolvation and consequently hinder the subsequent electron transfer between metal ions and carbonyl groups.<sup>[43]</sup> Conversely, the weaker interactions of  $\text{PF}_6^-$  with electrolyte solvents facilitate unobstructed charge transfer to amine groups.

To further investigate the cycled DAPT cathode, SEM, and XPS were employed to observe the surface changes during cycling and elucidate the reaction mechanism. SEM images of the cycled cathodes represent no obvious cracks or particle pulverization, demonstrating high structure integrity of the DAPT electrode (Figure S7). In the XPS analysis, the pristine

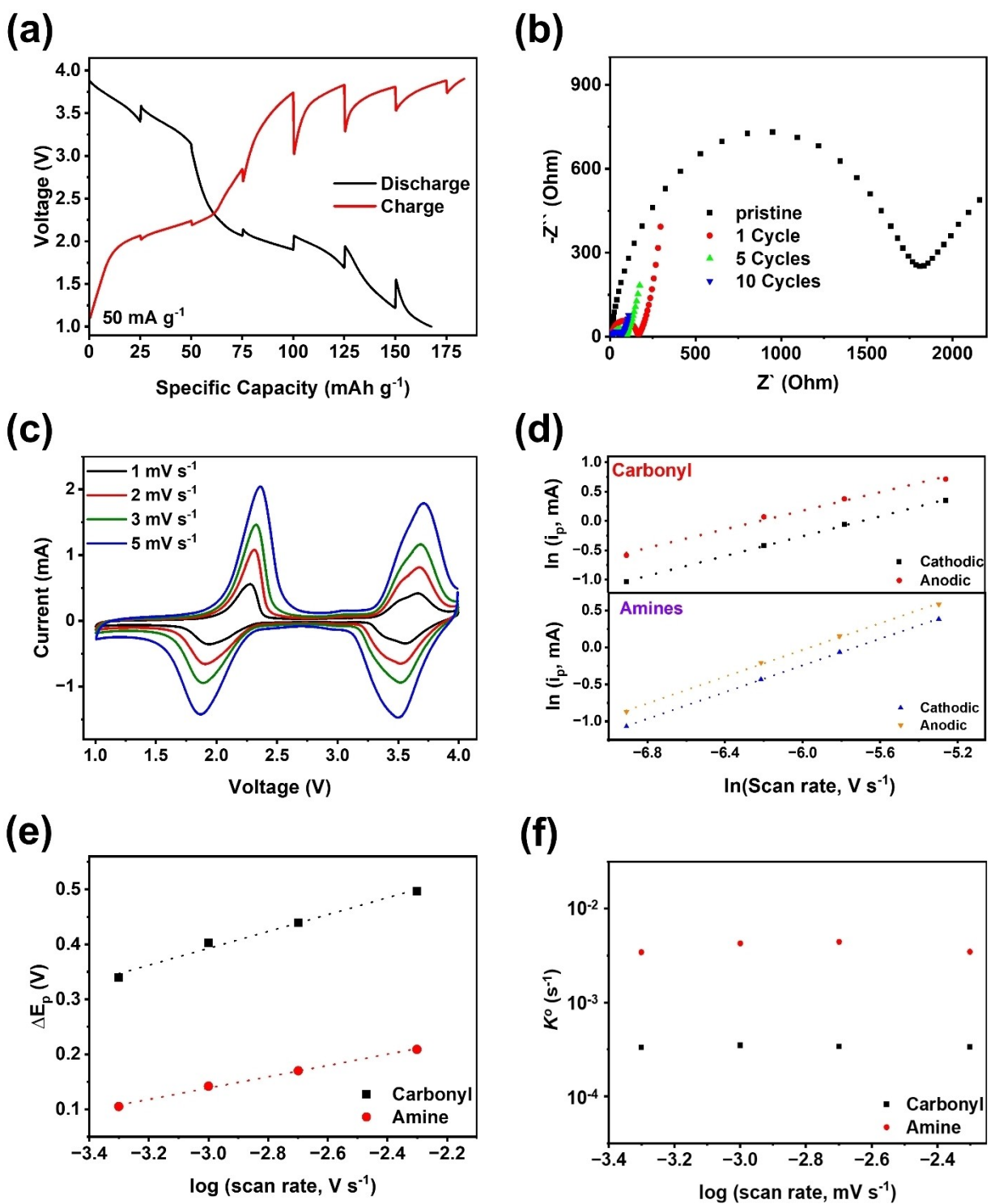


**Figure 3.** Kinetics study of the DAPT cathode; (a) rate capability at various current densities; (b) impedance analysis for pristine and cycled DAPT cathodes; (c) cyclic voltammograms at various scan rates from 0.1 to 1.0 mV s<sup>-1</sup>; (d) natural logarithm of peak current versus natural logarithm of scan rates for amine and carbonyl groups; (e) peak-to-peak separation ( $\Delta E_p$ ) versus log scan rates; (f) log reaction constant (k) versus log scan rates.

DAPT cathode and cycled cathodes, paused at different discharge or charge potentials during a cycle, were examined. The C 1s, O 1s, N 1s, and F 1s spectra for each distinct state are exhibited in the Figure 4. The F 1s spectrum of the pristine represents no peaks, confirming the absence of fluorine on the

surface. During the first discharge to 1.0 V, the C 1s spectrum exhibits an increased intensity of the C–O/C–N peak at 285.5 eV, indicating that carbonyl groups undergo a redox reaction with Na<sup>+</sup> ions and electrons.<sup>[44]</sup> Additionally, at 1.0 V, the O 1s spectrum represents peaks for C–O and Na KLL at

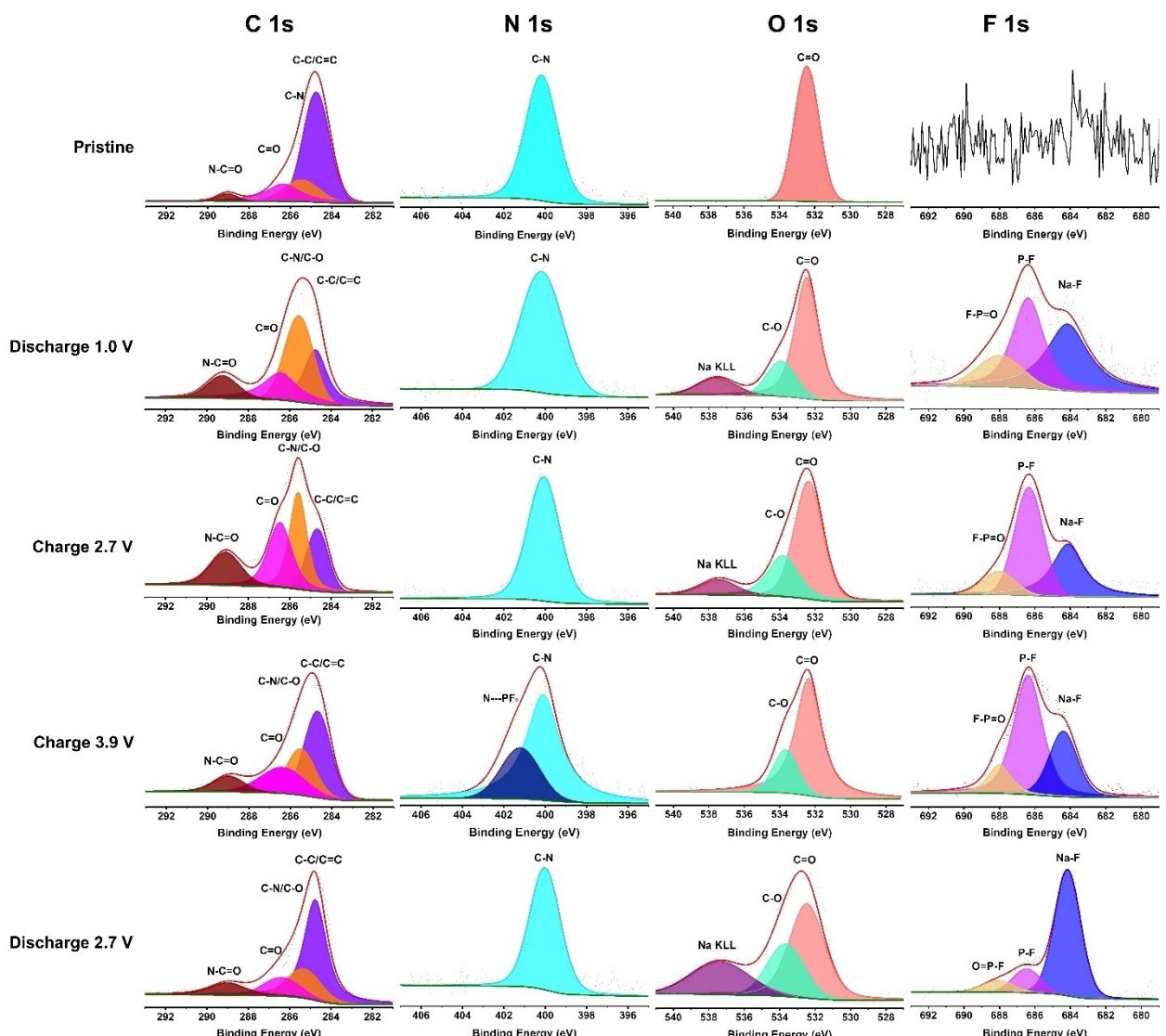
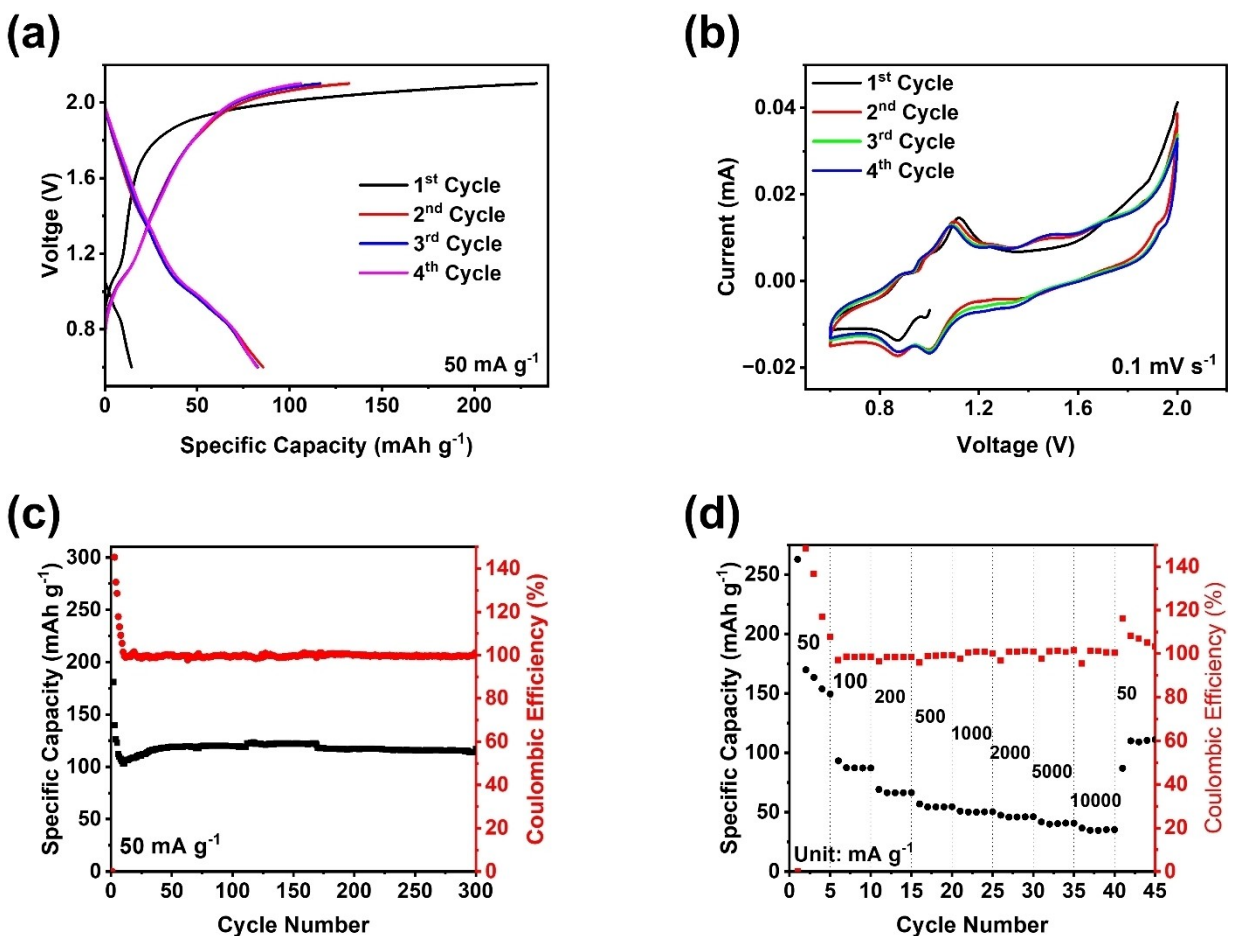


Figure 4. C 1s, N 1s, O 1s, and F 1s XPS spectra for the DAPT cathodes at various charge and discharge statuses.

355.9 eV and 537.5 eV, respectively, further confirming the sodiation reaction from carbonyl group.<sup>[45]</sup> In the C 1s spectrum, upon charging to 2.7 V, the intensity of C=O peaks at 286.4 eV is enhanced because of the re-formation of carbonyl groups after Na<sup>+</sup> ion extraction. Upon charging to 3.9 V, the intensity of the C-C/C-N peak in the C 1s spectrum is enhanced, demonstrating the reversible reaction between carbonyl groups and Na<sup>+</sup> ions. Meanwhile, in the N 1s spectrum at 3.9 V, a new peak is detected at 401.3 eV, representing the interaction between PF<sub>6</sub><sup>-</sup> ions and nitrogen cations following the anion insertion reaction.<sup>[46,47]</sup> In the O 1s spectrum at 3.9 V, Na KLL peak has disappeared, while the C=O peak is still detected, indicating that the species in the cathode electrolyte interphase (CEI) layer contain the C=O group. Upon discharge to 2.7 V, N<sup>+</sup>-PF<sub>6</sub><sup>-</sup> peak in the N 1s spectrum is not detected, demonstrating the reversible reaction between amine groups and PF<sub>6</sub><sup>-</sup>. The F 1s spectra exhibit the main F-containing components in the CEI.<sup>[48,49]</sup> After discharged from the pristine stage to 1.0 V, three

new peaks were detected, indicating the presence of Na-F, P-F, and F-P=O bonds. These three F 1s peaks were retained during subsequent charge and discharge, confirming their presence in the CEI. The formation of the CEI is further supported by the C=O bond manifested in the O 1s spectra.<sup>[50]</sup> Notably, the intensity of Na-F peak is strongest after 1 cycle at 2.7 V, proving that a NaF-rich CEI is formed.<sup>[51]</sup> Since NaF is a stable species, the formation of NaF-rich CEI contributes to the high performance of the DAPT cathode in NIBs.

Since the DAPT cathode exhibited superior electrochemical performances in NIBs, we further explored its application by studying performance in RABs. The ionic liquid-based electrolyte system (AlCl<sub>3</sub>:EMImCl) was used for electrochemical measurements with a cutoff window of 0.6–2.1 V (Al/Al<sup>3+</sup>). The first discharge in Figure 5a exhibited low capacity because only carbonyl groups from DAPT underwent redox reaction. After the initial cycles, both carbonyl and amine groups participated in the redox reactions, delivering the slopping redox plateaus



**Figure 5.** Electrochemical performances of the DAPT in RABs. (a) Galvanostatic charge-discharge curves at  $50 \text{ mA g}^{-1}$ ; (b) cyclic voltammograms at  $0.1 \text{ mV s}^{-1}$ ; (c) cycling performance in RABs; (d) rate capability at various current densities.

centered at  $\sim 1.3 \text{ V}$ . In the CV result (Figure 5b), three pairs of redox peaks centered at  $0.9 \text{ V}$ ,  $1.0 \text{ V}$ , and  $1.4 \text{ V}$  are observed, resulting in sloping plateaus in the galvanostatic charge-discharge curves. A reversible capacity of  $117.0 \text{ mAh g}^{-1}$  is retained for 300 cycles (Figure 5c), demonstrating good cyclic stability. The rate capability was also performed using same current densities as NIBs (Figure 5d). When the current density increases from  $50 \text{ mA g}^{-1}$  to  $10 \text{ A g}^{-1}$ , the specific capacity was decreased to  $34.6 \text{ mAh g}^{-1}$ . After returning to the  $50 \text{ mA g}^{-1}$ , the specific capacity of  $110.4 \text{ mAh g}^{-1}$  can be retained, indicating robust reaction kinetics in RABs. Therefore, the high performances of DAPT in NIBs and RABs demonstrate that this bipolar organic material is a promising cathode material for next-generation affordable and sustainable batteries.

## Conclusions

In summary, the bipolar organic material, comprising multiple carbonyl (n-type) and amine (p-type) groups, was successfully prepared through a facile condensation reaction. This material exhibits n-type and p-type characteristics in NIBs, delivering high redox potential, long cycle life, and fast reaction kinetics.

The extended conjugation structures in DAPT not only address the dissolution challenge of organic electrode material in the electrolyte but also enhance cyclic stability because of the  $\pi-\pi$  stacking with single-layer graphene. The kinetic study unravels that the electron transfer rate constant for the amine group is almost 10-fold higher than that of the carbonyl group, primarily attributed to solvation effect from electrolyte solution. The fast kinetics of DAPT in NIBs is attributed to the surface-reaction dominated mechanism. Additionally, the reaction mechanism and interphase were studied by XPS, confirming the reversible carbonyl/amine reactions and a NaF-rich CEI. Moreover, DAPT extends its high performance in NIBs to RABs and shows great promise for applications in multivalent batteries. Therefore, this research underscores the potential of developing bipolar organic cathode materials as a promising strategy to advance organic battery systems.

## Experimental

Perylenetetracarboxylic dianhydride (98%) and N1, N1-diphenylbenzene-1,4-diamine (99.92%) were purchased from TCI and Cheme Scene, respectively. Naphthalenetetracarboxylic dianhydride ( $> 97\%$ ) was purchased from TCI. Imidazole and dimethylforma-

mide (99.8%) were purchased from Sigma-Aldrich. The single-layer graphene was received from ACS materials. Carbon black (Super P, > 99%) and sodium alginate were purchased from Alfa Aesar and MP Biomedicals, respectively. Electrolyte solvents including ethylene carbonate (> 99%), diethyl carbonate (99%), and sodium hexafluorophosphate (> 99%) were received from Sigma Aldrich. Aluminum chloride (99.95%) and 1-ethyl-3-methylimidazolium chloride (99%) were purchased from Sigma Aldrich.

## Organic Materials Synthesis

In the DAPT synthesis, PTCDA (1 mmol) was dissolved in the liquid imidazole under inert gas, N<sub>2</sub>, at ~90°C. When temperature reached ~150°C, DPA (4 mmol) was transferred into the flask. Consequently, temperature was maintained at ~170°C. After 24 hours later, temperature was cooled down until ~60°C. The solution was crystallized. Ethanol was used to change solid into solution. The solution was filtered by funnel. Subsequently, filtrated solid particles were sonicated by DMF solvent (10 mL) four times and then particles were sonicated again by ethanol (10 mL) three times. Subsequently, the solid material was dried in the vacuum oven (80°C) overnight.<sup>[52]</sup>

In the NTDA synthesis, NTCDA (1 mmol) was dissolved in the DMF (10 mL) solvent which stirred for 24 hours with magnesium sulfate to remove water. The inert gas, N<sub>2</sub>, was flowing for one hour. Subsequently, the solution was heated until ~140°C. DPA sample was dissolved through 5 mL of DMF solvent and then injected into NTCDA solution. After that, temperature was maintained at ~140°C for 24 hours. The temperature was reduced to room temperature and then precipitate was collected. This precipitate was washed by tetrahydro furan, DMF, and ethanol. The obtained material was dried at 80°C in the vacuum oven overnight.<sup>[53]</sup>

## Characterization

Fourier-transform infrared (FTIR) spectra were recorded by Agilent Cary 630 FTIR Spectrometer. Raman spectra were obtained by Horiba XploRA PLUS Raman microscope with a 532 nm laser. Solid-state magic-angle spinning (MAS) NMR spectra of DAPT were recorded by a Bruker Avance NEO solid-state 500 MHz NMR spectrometer with a double resonance H/F-X probe. Cross polarization and magic-angle spinning was used for gathering <sup>13</sup>C, <sup>15</sup>N and <sup>17</sup>O spectra. These spectra were obtained by direct observation with MAS. Briefly, samples were packed in a 3.2 mm outer diameter zirconia rotor with Kel-F endcap spinning at 10 kHz. The π/2 pulse length was 2.5 us for the spectrum was 100 Hz. <sup>13</sup>C chemical shifts were referenced with respect to TMS by setting δ(<sup>13</sup>C)=0 ppm, <sup>15</sup>N chemical shift were referenced with respect to α-glycine by setting δ(<sup>15</sup>N)=33.4 ppm and <sup>17</sup>O chemical shifts were referenced with respect to water by setting δ(<sup>17</sup>O)=0 ppm. XPS measurement was conducted at a PHI 5000 VersaProbe II system (Physical Electronics) spectrometer, which is equipped with a hemispherical analyzer. The XPS peaks were referenced to the C–C bond (284.4 eV) of C 1s as internal binding energy standard.<sup>[46,54]</sup>

Scanning electron microscopy (SEM) image were obtained by JEOL JSM-IT500HR instrument.

## Electrochemical Measurement

DAPT or NTDA material was mixed with single-layer graphene (Gr) for one hour with mass ratio 6:2. Subsequently, 10 wt% of carbon black (Super P) and 10 wt% of sodium alginate solution were added to make a slurry. The slurry was cast on carbon-coated aluminum film for NIBs or on molybdenum film for RABs using a doctor blade and dried in a vacuum oven at 80°C overnight. After that, dried film was punched out using a round hollow puncher, resulting in an average mass loading of ~1.3 mg cm<sup>-2</sup>. To prepare high mass loading electrode (~5.0 mg cm<sup>-2</sup>), active material was mixed with carbon black and then polytetrafluoroethylene (PTFE) binder was added with 8:1:1 mass ratio. The powder sample was turned into a film and stainless-steel mesh was used as current collector instead of aluminum film. These high mass loading samples were used for Raman spectrometer. The DAPT electrode for RABs was prepared using graphene and sodium alginate with 5:4:1 mass ratio to form a slurry. This slurry was casted onto Mo foil using a doctor blade and dried in a vacuum oven at 80°C overnight. All assembling batteries was proceeded under Argon-filled glove box, maintained H<sub>2</sub>O < 0.1 ppm and O<sub>2</sub> < 0.1 ppm. The coin cells of sodium batteries were assembled using sodium metal as the counter electrode and 1 M NaPF<sub>6</sub> in ethylene carbonate (EC) and diethylene carbonate (DEC) with 1:1 volumetric ratio was used as electrolyte in the NIBs cell. To assemble RABs, swagelok type cells were used with aluminum film as counter electrode and ionic electrolyte, AlCl<sub>3</sub> and EMImCl with (1.5:1 mol), was used.<sup>[55,56]</sup>

The theoretical capacity (C<sub>th</sub>) of DAPT and NTDA have been calculated using mathematic equations, C<sub>th</sub>=(nxF)/M. The n is the number of electrons which participates redox reaction, F is the Faraday constant, and M is the molecular weight of samples. Based on the redox reaction mechanism, the theoretical capacity of DAPT and NTDA are 122.4 mAh g<sup>-1</sup> and 142.5 mAh g<sup>-1</sup>, respectively.

The electrochemical performance was verified using Landt instruments or the Arbin battery test system. The cyclic voltammogram for NIBs were recorded using CHI 760E Biopotentiostat from CH Instruments with a scan rate of 1.0–5.0 mVs<sup>-1</sup>. The cyclic voltammograms were iR-corrected to minimize the impacts of electrolyte resistance on the determined electrode kinetics.<sup>[57]</sup> The electrolyte resistance was obtained from EIS. The cyclic voltammograms for RABs were recorded through the Gamry Reference 1010E Potentiostat/Galvanostat/ZRA with scan rate of 0.1–1.0 mVs<sup>-1</sup>. Impedance analysis was performed using CHI 760E from CH instrument.

## Acknowledgements

This work was supported by the US National Science Foundation Award No. 2419947. The authors also acknowledge the

support from the George Mason University Quantum Science & Engineering Center. We gratefully acknowledge support from the Post Test Facility at Argonne National Laboratory, which is operated for the DOE Vehicle Technologies Office (VTO) by UChicago Argonne, LLC, under contract number DE-AC02-06CH11357. We thank the NSF (NSF-1726058) for funding a solid-state NMR spectrometer at the University of Maryland, College Park.

### Conflict of Interests

The authors declare no conflict of interest.

### Data Availability Statement

The data that support the findings of this study are available from the corresponding author upon reasonable request.

- [1] K. Balaji, M. Rabiei, *Sustain. Energy Technol. Assessments* **2022**, *51*, 2213–1388.
- [2] T. Kim, W. Song, D. Y. Son, L. K. Ono, Y. Qi, *J. Mater. Chem. A* **2018**, *30* (33), 2942–2964.
- [3] C. R. Jarvis, M. J. Lain, M. V. Yakovleva, Y. Gao, *J. Power Sources* **2006**, *162* (2), 800–802.
- [4] K. Qin, K. Holguin, M. Mohammadiroudbari, J. Huang, E. Y. Kim, R. Hall, C. Luo, *Adv. Funct. Mater.* **2021**, *31* (15), 2009694.
- [5] T. L. Kulova, V. N. Fateev, E. A. Seregina, A. S. Grigoriev, *Int. J. Electrochem. Sci.* **2020**, *15* (8), 7242–7259.
- [6] L. Sun, Y. Liu, R. Shao, J. Wu, R. Jiang, Z. Jin, *Energy Storage Mater.* **2022**, *46*, 382–502.
- [7] C. Vaalma, D. Buchholz, M. Weil, S. Passerini, *Nat. Rev. Mater.* **2018**, *3*, 18013.
- [8] K. Zhang, K. O. Kirlikovali, J. N. Sug, J. W. Choi, H. W. Jang, R. S. Varma, O. K. Farha, M. Shokouhimehr, *ACS Appl. Energ. Mater.* **2020**, *3* (7), 6019–6035.
- [9] Z. A. Zafar, S. Imtiaz, R. Razaq, S. Ji, T. Huang, Z. Zhang, Y. Huang, J. A. Anderson, *J. Mater. Chem.* **2017**, *5*, 5646–5660.
- [10] J. J. Shea, C. Luo, *ACS Appl. Mater. Interfaces* **2020**, *12*, 5361–5380.
- [11] Y. Lu, Q. Zhang, L. Lin, N. Zhiqiang, C. Jun, *Chem* **2018**, *4* (12), 2786–2813.
- [12] K. Holguin, M. Mohammadiroudbari, K. Qin, C. Luo, *J. Mater. Chem. A* **2021**, *9*, 19083–19115.
- [13] S. Lee, J. Hong, K. Kang, *Adv. Energy Mater.* **2020**, *10* (30), 2001445.
- [14] X. Feng, X. Wu, X. Chen, J. Yuan, S. S. Lv, B. Ren, X. Sun, E. Liu, S. Tan, P. Gao, *Energy Storage Mater.* **2021**, *42*, 454–463.
- [15] Q. Yum, Z. Xue, M. Li, P. Qiu, C. Li, S. Wang, J. Yu, H. Nara, J. Na, Y. Yamauchi, *Adv. Energy Mater.* **2021**, *11* (7), 2002523.
- [16] Y. Lu, J. Chen, *Nat. Chem. Rev.* **2020**, *4*, 127–142.
- [17] B. M. Peterson, C. N. Gannett, L. M. Zambrano, B. P. Fors, H. Abruna, *ACS Appl. Mater. Interfaces* **2021**, *13* (6), 7135–7141.
- [18] T. Liu, C. Kim, B. Lee, S. Jin, M. J. Lee, M. Li, S. Noda, S. S. Jang, S. W. Lee, *ACS Appl. Energ. Mater.* **2020**, *3* (4), 3728–3735.
- [19] B. Robert, *Photosynth. Res.* **2009**, *101*, 147–155.
- [20] D. J. Kim, D. J. Yoo, M. T. Otley, A. Prokofjevs, C. Pezzato, M. Owczarek, S. J. Lee, J. W. Choi, J. F. Stoddart, *Nat. Energy* **2018**, *4*, 51–59.
- [21] J. Xie, Y. C. Lu, *Nat. Mater.* **2021**, *20*, 581–583.
- [22] Z. Song, H. Zhou, *Energy Environ. Sci.* **2013**, *6*, 2280.
- [23] D. A. Tenne, S. Park, T. U. Kampen, A. Das, R. Scholz, D. R. T. Zahn, *Phys. Rev. B* **2000**, *61* (21), 14564.
- [24] R. Scholtz, A. Yu Kobitski, T. U. Kampen, M. Schreiber, D. R. T. Zahn, *Phys. Rev. B* **1999**, *61* (20), 13659.
- [25] P. Bertani, J. Raya, B. Bechinger, *Solid State Nucl. Magn. Reson.* **2014**, *61*, 15–18.
- [26] J. M. D. Rosa, A. Z. Miller, H. Knicker, *Sci. Rep.* **2018**, *8*, 2896.
- [27] G. Wu, *Prog. Nucl. Magn. Reson. Spectrosc.* **2008**, *52*, 118–169.
- [28] M. C. Biesinger, *Appl. Surf. Sci.* **2022**, *597*, 153681.
- [29] M. Mohammadiroudbari, K. Qin, C. Luo, *Batteries & Supercaps* **2022**, *5* (6), e202200021.
- [30] S. Zheng, L. Miao, T. Sun, L. Li, T. Ma, J. Bao, Z. Tao, J. Chen, *J. Mater. Chem. A* **2021**, *9*, 2700–2705.
- [31] E. Y. Kim, M. Mohammadiroudbari, F. Chen, Z. Yang, C. Luo, *ACS Nano* **2024**, *18* (5), 4159–4169.
- [32] Q. Zhao, Y. Lu, J. Chen, *Adv. Energy Mater.* **2016**, *7* (8), 1601792.
- [33] K. Qin, K. Holguin, M. Mohammadiroudbari, C. Luo, *Chem. Commun.* **2021**, *57*, 2360–2363.
- [34] P. Lu, Y. Sun, H. Xiang, X. Liang, Y. Yu, *Adv. Eng. Matr.* **2018**, *8* (8), 1702434.
- [35] G. Leftheriotis, S. Papaefthimiou, P. Tianoulis, *Solid State Ionics* **2007**, *178*, 259–263.
- [36] X. Chen, X. Q. Zhang, H. R. Li, Q. Zhang, *Batteries & Supercaps* **2018**, *2* (2), 128–131.
- [37] C. Luo, E. Hu, K. J. Gaskell, X. Fan, T. Gao, C. Cui, S. Ghose, X. Q. Yang, C. Wang, *PNAS* **2020**, *117*, 26.
- [38] R. J. Forster, L. R. Faulkner, *J. Am. Chem. Soc.* **1994**, *116*, 5453–5461.
- [39] G. P. Stevenson, R. E. Baker, G. F. Kennedy, A. M. Bond, D. J. Gavaghan, K. Gillow, *Phys. Chem. Chem. Phys.* **2013**, *15*, 2210–2221.
- [40] E. Laviron, *J. Electroanal. Chem. Interfacial Electrochem.* **1979**, *101* (1), 19–28.
- [41] Z. Tian, Y. Zou, G. Liy, Y. Wang, J. Y. Ming, H. N. Alshareef, *Adv. Sci.* **2022**, *9* (22), 2201207.
- [42] K. W. Schroder, A. G. Dylla, L. D. Bishop, E. R. Kamilar, J. Saunders, L. J. Webb, K. J. Stevenson, *J. Phys. Chem. Lett.* **2015**, *6*, 2888.
- [43] N. Sahai, D. A. Sverjensky, *GCA* **1997**, *61*, 2827.
- [44] S. Kundu, Y. Wang, W. Xia, M. Muhler, *J. Phys. Chem. C* **2008**, *112* (43), 16869–16878.
- [45] C. Andrello, T. Grouder, L. Favergeon, L. Desgranges, E. T. Chitrova, L. Havela, R. J. M. Konings, R. Eloirdi, *J. Nucl. Matr.* **2021**, *545*, 152646.
- [46] M. Mohammadiroudbari, J. Huang, E. Y. Kim, Z. Yang, F. Chen, C. Luo, *J. Matr. Chem. A* **2023**, *11*, 16636–16647.
- [47] M. R. Raj, N. Kim, G. Lee, *Sustain. Energy Fuels* **2021**, *5*, 175–187.
- [48] Y. F. Pulido, C. Blanco, D. Ansean, V. M. Garcia, F. Ferrero, M. Valledor, *Measurement* **2017**, *106*, 1–11.
- [49] L. Wang, J. Zhao, X. He, J. Gao, J. Li, C. Wan, C. Jiang, *Int. J. Electrochem. Sci.* **2012**, *7* (1), 345–353.
- [50] S. Nagarajan, C. Weiland, S. Hwang, M. Balasubramanian, L. M. R. Arava, *Chem. Mater.* **2022**, *34*, 4857–4601.
- [51] Z. Tai, Y. Liu, Z. Yu, Z. Lu, O. Bondarchuk, Z. Peng, L. Liu, *Nano Energy* **2022**, *94*, 106947.
- [52] B. Deng, J. Li, H. Shang, W. Liu, Q. Wan, M. Chen, M. Qu, G. Peng, *Ionics* **2020**, *26*, 2247–2257.
- [53] M. Mohammadiroudbari, S. Li, J. Huang, Z. Yang, F. Chen, L. Cheng, C. Luo, *Batteries & Supercaps* **2024**, *7*, e202300472.
- [54] M. Zarrabeitia, M. C. Cabana, M. A. M. Marquez, *Electrochim. Acta* **2021**, *372*, 137846.
- [55] D. J. Yoo, M. Heeney, F. Glockhofer, J. W. Choi, *Nat. Commun.* **2021**, *12*, 2386.
- [56] K. Qin, S. Tan, M. Mohammadiroudbari, Z. Yang, X. Q. Yang, E. Hu, C. Luo, *Nano Energy* **2022**, *101*, 107554.
- [57] T. Hottinen, M. Mikkola, T. Mennola, P. Lund, *J. Power Sources* **2003**, *118* (1–2), 183–188.

Manuscript received: May 15, 2024

Revised manuscript received: June 11, 2024

Accepted manuscript online: June 14, 2024

Version of record online: July 29, 2024